Radiation Physics and Chemistry 96 (2014) 107–114

Contents lists available at ScienceDirect

Radiation Physics and Chemistry

journal homepage: www.elsevier.com/locate/radphyschem

# Accurate 3D reconstruction by a new PDS-OSEM algorithm for HRRT

Tai-Been Chen [a], Henry Horng-Shing Lu [b], Hang-Keun Kim [c], Young-Don Son [c], Zang-Hee Cho [c,*]

[a] Department of Medical Imaging and Radiological Sciences, I-Shou University, Taiwan, ROC
[b] Institute of Statistics, National Chiao Tung University, Taiwan, ROC
[c] Neuroscience Research Institute, Gachon University, South Korea

## HIGHLIGHTS

- The PDS-OSEM reconstructs PET images with iteratively compensating random and scatter corrections from prompt sinogram.
- The PDS-OSEM can reconstruct PET images with low count data and data contaminations.
- The PDS-OSEM provides less noise and higher quality of reconstructed images than those of OP-OSEM algorithm in statistical sense.

## ARTICLE INFO

*Article history:*
Received 9 August 2013
Accepted 17 September 2013
Available online 25 September 2013

*Keywords:*
HRRT
PET
OP-OSEM
PDS-OSEM
Time Activity Curve
Average Sum of Square Error

## ABSTRACT

State-of-the-art high resolution research tomography (HRRT) provides high resolution PET images with full 3D human brain scanning. But, a short time frame in dynamic study causes many problems related to the low counts in the acquired data. The PDS-OSEM algorithm was proposed to reconstruct the HRRT image with a high signal-to-noise ratio that provides accurate information for dynamic data. The new algorithm was evaluated by simulated image, empirical phantoms, and real human brain data. Meanwhile, the time activity curve was adopted to validate a reconstructed performance of dynamic data between PDS-OSEM and OP-OSEM algorithms. According to simulated and empirical studies, the PDS-OSEM algorithm reconstructs images with higher quality, higher accuracy, less noise, and less average sum of square error than those of OP-OSEM. The presented algorithm is useful to provide quality images under the condition of low count rates in dynamic studies with a short scan time.



## 1. Introduction

The high-resolution research tomography (HRRT) scanner for positron emission tomography (PET) can provide high-resolution functional brain images with a spatial resolution close to 2.5 mm (Cho et al., 2007, 2008). HRRT can be used for molecular imaging such as neurotransmitter, neuroreceptor, and neurotransporter studies (Leroy et al., 2007) in human brain function by using dynamic scanning. However, the quality of HRRT images in the dynamic studies is hindered by the limitations of reconstructed algorithms and the low counts of each bin, which are related to the short scanning time. Implementations of generalized EM algorithms for PET reconstruction have been proposed in the literature. The ordinary Poisson ordered subset expectation maximum (OP-OSEM) (Van Velden et al., 2008), ordinary Poisson list mode expectation maximum (OP-LMEM) (Cheng et al., 2007), attenuation correction ordered subset expectation maximum (AC-OSEM) (Bengel et al., 1997), iterative correction of random events with MLE-EM algorithm (PDEM) (Chen et al., 2008), and improved reconstruction techniques with faster computational time (Hong et al., 2007) were presented in recent. In the reconstruction methods based on OSEM algorithms, the algorithms are often combined with attenuation, random, and scatter corrections. The random and scatter corrections used in these OSEM algorithms are often performed by two approaches. The first approach considers the prompt sinogram minus the delayed and scatter data, whereas the second approach applies averages of delayed and scatter data in the step of forward projection. In the first approach, lots of LORs became zeros after subtracting the random and scatter data from the prompt sinogram. Also, the inaccurate scatter estimation will affect volume uniformity (De Jong et al., 2007, Rahmim et al., 2005). In the second approach, it is inefficient to reduce noise for iteratively reconstructed PET images (Rahmim et al., 2005). Furthermore, the conventional EM algorithm usually provides poor image quality because the random and scatter data for dynamic studies are subtracted from prompt data when lower count rates are acquired from PET in a few seconds. In addition,

* Correspondence to: 1198 Kuwol-dong, Namdong-gu, Incheon 405-760, South Korea. Tel.: +82 32 460 2083; fax: +82 32 460 2081.
*E-mail address:* zcho@gachon.ac.kr (Z.-H. Cho).

0969-806X/$ - see front matter © 2013 Elsevier Ltd. All rights reserved.
http://dx.doi.org/10.1016/j.radphyschem.2013.09.006

the scatter fraction determination was affected by random and true coincidence events under different low level count rates (Eriksson et al., 2005). In the dynamic study, the random and scattering events are estimated by using expected mean scatter, random counts, and estimated scatter fraction to adjust the bias iteratively (Cheng et al., 2007). Therefore, it is very important to improve the precision and the accuracy of the iteratively reconstructed HRRT images with improved methods of random and scatter corrections (Van Velden et al., 2008, 2009).

The proposed algorithm combines prompt and delayed sinograms with simulated scatter sinogram for HRRT reconstruction based on the joint Poisson model and OSEM algorithm; therefore, it is called PDS-OSEM. The PDS-OSEM not only improves the accuracy of reconstructed images, it also reduces image bias at low level rates. Meanwhile, PDS-OSEM can be easily implemented by making a few changes in the existing code of the conventional OSEM algorithm. The derivation of PDS-OSEM will be reported in Appendix A. Simulation and empirical studies will be conducted to evaluate the performance between PDS- and OP-OSEM. The Poisson assumption was used for simulated scatter sinogram because of the easy implementation of the algorithm and the approximation to a normal distribution as a parameter of Poisson increases to infinity. Consequently, the derived image-reconstruction algorithms can generate images that help physicians diagnose disease accurately (Barrett, 1990, Barrett et al., 1993, 1995). Therefore, the Poisson model provides a useful and simplified modeling technique for image reconstruction.

## 2. Methodology and materials

### 2.1. The algorithm of PDS-OSEM

We will assume three independent Poisson models for prompt, delay, and scatter sinogram as shown in Eqs. (1–3).

$$n_p^*(d) \sim Poisson(\lambda^*(d)), \tag{1}$$

$$n_r^*(d) \sim Poisson(\lambda_r^*(d)), \tag{2}$$

$$n_s^*(d) \sim Poisson(\lambda_s^*(d)), \tag{3}$$

where $\lambda^*(d)=\lambda_t^*(d)+\lambda_r^*(d)+\lambda_s^*(d)=\sum_b P(b,d)\{\lambda_t(b)+\lambda_r(b)+\lambda_s(b)\}$, $b=1, 2, \ldots, B$ for the pixel index (location) of reconstructed image, and $d=1, 2, \ldots, D$ for the bin index (projection line) in the sinogram. The notation $n_p^*(d)$ denotes the number of coincidence events in the prompt sinogram for all of the detection tubes formed by two detectors with Poisson parameter $\lambda^*(d)$. $\lambda_t^*(d)$ denotes the number of forward projections by true image $\lambda_t(b)$. $n_r^*(d)$ denotes the number of random coincidence events in the delay sinogram with Poisson parameter $\lambda_r^*(d)$. $n_s^*(d)$ denotes the number of scattering coincidence events using single scatter simulation (Watson, 2000) (or Monte Carlo simulation) with Poisson parameter $\lambda_s^*(d)$. $P(b,d)$ denotes the elements of the system matrix which is the probability that an event generated at $b$th pixel is detected along $d$th detection tube (or $d$th line of response). The parameters of $\lambda_t(b)$,$\lambda_r(b)$, and $\lambda_s(b)$ are unknown and have to be estimated. The parameters of $\lambda_t(b)$ represent the intensities of true coincidence events at $b$th pixel in reconstructed image. Note that $\lambda_r(b)$ and $\lambda_s(b)$ do not physically exist. They are only derived values by $\lambda_r^*(d)$ and $\lambda_s^*(d)$ in the presented algorithm. As scatter events arise from the scattering effect of the photon pairs emitted in the annihilations of photons and nearby electrons, the Poisson distribution could be used to model the random phenomena of these annihilations. These assumptions can indeed lead to the closed form solution in the EM algorithm for the estimates of true, random and scatter events. Hence, these assumptions provide a useful and simplified model for the setup of complete data space.

The log-likelihood of the above observed data in prompt, delay, and scatter sinograms are listed as Eq. (4).

$$\begin{aligned} l_{in}(\lambda_t(b),\lambda_r(b),\lambda_s(b)) \propto & \sum_{d=1}^{D}\{[-\sum_{b=1}^{B}P(b,d)(\lambda_t(b)+\lambda_r(b)+\lambda_s(b)] \\ & +n_p^*(d)\log(\sum_{b=1}^{B}P(b,d)(\lambda_t(b)+\lambda_r(b)+\lambda_s(b))\} \\ & +\sum_d\{[-\sum_{b=1}^{B}P(b,d)\lambda_r(b)]+n_r^*(d)\log(\sum_{b=1}^{B}P(b,d)\lambda_r(b))\} \\ & +\sum_d\{[-\sum_{b=1}^{B}P(b,d)\lambda_s(b)]+n_s^*(d)\log(\sum_{b=1}^{B}P(b,d)\lambda_s(b))\} \end{aligned} \tag{4}$$

Because the MLE is difficult to obtain by maximizing the above equation numerically, we can apply the EM algorithm as follows. First, the observed data in prompt, delay, and scatter sinograms for all detector pairs are regarded as incomplete data. The EM algorithm needs to specify the complete data. One possible and simplified model for the complete data for reconstruction of PET is as follows Eqs. (5–9).

$$n_p(b,d) \sim Poisson(p(b,d)\lambda_t(b)), \tag{5}$$

$$n_p^r(b,d) \sim Poisson(P(b,d)\lambda_r(b)), \tag{6}$$

$$n_p^s(b,d) \sim Poisson(P(b,d)\lambda_s(b)), \tag{7}$$

$$n_r(b,d) \sim Poisson(P(b,d)\lambda_r(b)), \tag{8}$$

$$n_s(b,d) \sim Poisson(P(b,d)\lambda_s(b)), \tag{9}$$

where $n_p(b,d)$ is the number of emissions detected by $d$th tube at $b$th pixel of true image, $n_p^r(b,d)$ is the number of accidental (or random) coincidence (AC or RC) events detected by $d$th tube at $b$th pixel of true image, and $n_p^s(b,d)$ is the number of scattering coincidence events at $b$th pixel of true image in $d$th tube derived from a scatter estimation, such as single scatter simulation or Monte Carlo simulation. $n_r(b,d)$ is the assumed unobserved number of accidental (or random) coincidence (AC or RC) events detected by $d$th tube from $b$th pixel, and $n_s(b,d)$ is the assumed unobserved number of scattering coincidence events detected by $d$th tube at $b$th pixel. Note that we assume the estimated scatter coincidence follows the Poisson model. We will assume that $n_p(b,d)$, $n_p^r(b,d)$, $n_p^s(b,d)$, $n_r(b,d)$, and $n_s(b,d)$ are statistically independent. Thus, $n_p^*(d)=\sum_{b=1}^{B}n_p(b,d)+n_p^r(b,d)+n_p^s(b,d)$, $n_r^*(d)=\sum_{b=1}^{B}n_r(b,d)$, and $n_s^*(d)=\sum_{b=1}^{B}n_s(b,d)$. The E-step will compute the conditional expectation of the log-likelihood of complete data, given the observed incomplete data and old values (i.e., $k=0$) of parameters. The starting value of $\lambda_t^k(b)$ is initialized by FBP, and the starting values of $\lambda_r^k(b)$ and $\lambda_s^k(b)$ are initialized to 0.05. According to models Eqs. (5–9), the joint log-likelihood function of the complete data is given as in Eq. (10) and the constant terms are omitted.

$$\begin{aligned} L(\lambda_t(b),\lambda_r(b),\lambda_s(b)) \propto & \sum_d\sum_b\{n_p(b,d)\log(P(b,d)\lambda_t(b))-P(b,d)\lambda_t(b)\} \\ & +\sum_d\sum_b\{n_p^r(b,d)\log(P(b,d)\lambda_r(b))-P(b,d)\lambda_r(b)\} \\ & +\sum_d\sum_b\{n_p^s(b,d)\log(P(b,d)\lambda_s(b))-P(b,d)\lambda_s(b)\} \\ & +\sum_d\sum_b\{n_r(b,d)\log(P(b,d)\lambda_r(b))-P(b,d)\lambda_r(b)\} \\ & +\sum_d\sum_b\{n_s(b,d)\log(P(b,d)\lambda_s(b))-P(b,d)\lambda_s(b)\}. \end{aligned} \tag{10}$$

The conditional distribution of $n_p(b,d)$, $n_p^r(b,d)$, $n_p^s(b,d)$, $n_r(b,d)$, and $n_s(b,d)$ given as observed data are shown in the Appendix A. The M-step will determine $\lambda_t^{k+1}(b)$, $\lambda_r^{k+1}(b)$, and $\lambda_s^{k+1}(b)$ as the solutions that maximize the function of the expectation of the complete

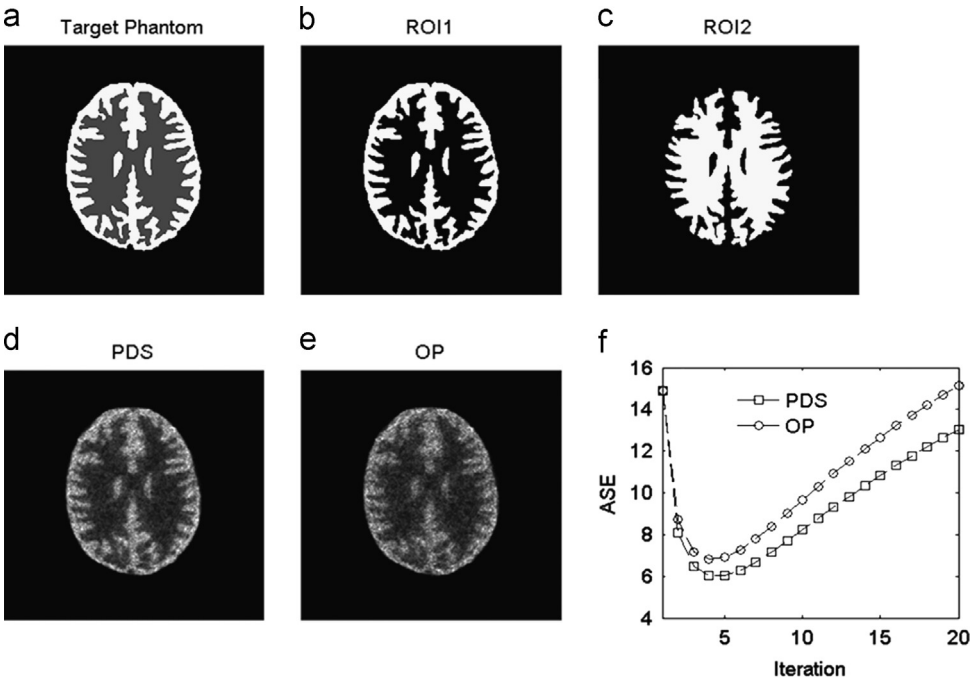


**Fig. 1.** This figure shows the target image with an imputed pixel value of 50 for the white part and 10 for the gray part (a). The two ROIs were selected to compare the SNR between PDS-and OP-OSEM (b and c). The bottom row shows the reconstructed images with stopping rules determined by the minimum averaging square of error (ASE) (d and e). Both PDS- and OP-OSEM stopped at the 4th iteration (f). A smaller ASE means that the reconstructed image resembles the target image.

log-likelihood. This can be achieved now by taking the first derivatives equal to zero. The solutions are shown in Eqs. (11–13) and detailed derivations are shown in the Appendix A.

$$\lambda_t^{k+1}(b)=\frac{\lambda_t^k(b)}{\sum_{d=1}^{D}P(b,d)}\sum_{d=1}^{D}\frac{n_p^*(d)p(b,d)}{\sum_{b'=1}^{B}p(b',d)[\lambda_t^k(b')+\lambda_r^k(b')+\lambda_s^k(b')]}, \tag{11}$$

$$\lambda_r^{k+1}(b)=\frac{\lambda_r^k(b)}{2\sum_d P(b,d)}\sum_d\left[\frac{n_p^*(d)P(b,d)}{\sum_{b'=1}^{B}p(b',d)[\lambda_t^k(b')+\lambda_r^k(b')+\lambda_s^k(b')]}+\frac{n_r^*(d)P(b,d)}{\sum_{b'=1}^{B}p(b',d)\lambda_r^k(b')}\right], \tag{12}$$

$$\lambda_s^{k+1}(b)=\frac{\lambda_s^k(b)}{2\sum_d P(b,d)}\sum_d\left[\frac{n_p^*(d)P(b,d)}{\sum_{b'=1}^{B}p(b',d)[\lambda_t^k(b')+\lambda_r^k(b')+\lambda_s^k(b')]}+\frac{n_s^*(d)P(b,d)}{\sum_{b'=1}^{B}p(b',d)\lambda_s^k(b')}\right], \tag{13}$$

where $k=1, 2, \ldots, K$, represents the iteration number after the initial number of zero.

The MLE-EM algorithm for the joint model of prompt, delay, and scattered sinograms is described in Eqs. (11–13); henceforth, it will be called the *PDS-OSEM* algorithm. This novel approach not only reconstructs HRRT but updates estimated true intensities with iteratively corrected random and scattering noise. The simulated, empirical, and dynamic data were applied to compare the performance between the presented method and OP-OSEM.

### 2.2. The algorithm of OP-OSEM

The algorithm of ordinary Poisson OSEM (OP-OSEM) is presented in Eq. (14). OP-OSEM is an iterative reconstructed method that adopts observed random and scattered coincidence data without updated information of random and scattered noise from a prompt sinogram in each iteration. The advantage of this algorithm is using whole data to reconstruct HRRT, as does PDS-OSEM. However, PDS-OSEM iteratively updates the estimated noise of random and scatter from $n_r^*(d)$, $n_s^*(d)$, and $n_p^*(d)$. This capability however will increase the computational cost of PDS-OSEM compared with that of OP-OSEM. On the other hand, reconstructed HRRT images provided by PDS-OSEM will have less noise and better quality than those of OP-OSEM.

$$\lambda_t^{k+1}(b)=\frac{\lambda_t^k(b)}{\sum_{d=1}^{D}P(b,d)}\sum_{d=1}^{D}\frac{n_p^*\ (d)P(b,d)}{\sum_{b'=1}^{B}p(b',d)\lambda_t^k(b')+n_r^*(d)+n_s^*(d)} \tag{14}$$

### 2.3. Materials

#### 2.3.1. HRRT

HRRT is the state-of-the-art human brain-imaging device of PET. HRRT not only provides functional and metabolic images; it also generates high spatial resolution down to 2.5 mm full width at half maximum (FWHM) (Wienhard et al., 2002). HRRT has a diameter 46.9 cm and an axial FOV 25.2 cm. The smaller system diameter and the longer axial FOV can improve system sensitivity. HRRT utilizes the smallest detector size currently available, with a dimension of 2.3 mm by 2.3 mm. It applies the depth of interaction (DOI) scheme using dual detector layers, in which LSO and LYSO layers, with the depth of 10 mm each (De Jong et al., 2007, Schmand et al., 1998, Eriksson et al., 2002, Astakhov et al., 2003) are combined. This scheme improves the energy resolution and the coincident efficiency. The gantry includes eight detector heads and each detector head includes $13\times 9$ detector blocks. Each block has $8\times 8$ detectors of double layers. Hence, the total number of scintillation detector crystals is 119,808. Also, each detector of HRRT can match the opposite five heads, corresponding to 74,880 detectors, and form a total of 4.48 billion LORs (lines of response) (Cho et al., 2008).

#### 2.3.2. Simulation, phantom, and human dynamic study

A Hoffman digital brain image simulated in 2D was used to evaluate and investigate the accuracy of reconstructed images. The image size of the target image is $256\times 256$ pixels. The two ROIs selected from the target image are shown in Fig. 1. The intensity is 50 and 10 for the 1st and 2nd ROI, respectively. Meanwhile, the

**Table 1**
Data from ROI analysis of OP-OSEM and PDS-OSEM are shown. Compared with OP-OSEM, the PDS-OSEM algorithm improves the performance of SNR, average, and ASE by 20 realizations of target image. Note, the Average Relative Performance (ARP) is defined as 100% × [(a)−(c)]/(c) and 100% × [(b)−(d)]/(d).

| Realization | Average in ROI | | | | SNR | | | | Minimum ASE | |
|---|---|---|---|---|---|---|---|---|---|---|
| | PDS | | OP | | PDS | | OP | | PDS | OP |
| | ROI 1 | ROI 2 | ROI 1 | ROI 2 | ROI 1 | ROI 2 | ROI 1 | ROI 2 | | |
| 1 | 41.42 | 14.59 | 40.47 | 16.14 | 3.28 | 2.30 | 2.89 | 2.20 | 6.01 | 6.79 |
| 2 | 41.78 | 14.64 | 40.69 | 16.23 | 3.28 | 2.26 | 2.89 | 2.20 | 6.00 | 6.80 |
| 3 | 41.66 | 14.72 | 40.46 | 16.27 | 3.27 | 2.34 | 2.87 | 2.28 | 6.00 | 6.81 |
| 4 | 41.48 | 14.70 | 40.38 | 16.28 | 3.25 | 2.37 | 2.88 | 2.26 | 6.01 | 6.81 |
| 5 | 41.85 | 14.69 | 40.77 | 16.24 | 3.26 | 2.32 | 2.87 | 2.24 | 5.98 | 6.78 |
| 6 | 41.84 | 14.78 | 40.88 | 16.41 | 3.27 | 2.27 | 2.91 | 2.19 | 6.02 | 6.81 |
| 7 | 41.65 | 14.76 | 40.71 | 16.36 | 3.32 | 2.32 | 2.95 | 2.25 | 5.98 | 6.74 |
| 8 | 41.96 | 14.60 | 40.96 | 16.19 | 3.30 | 2.28 | 2.88 | 2.22 | 5.95 | 6.75 |
| 9 | 41.76 | 14.89 | 40.93 | 16.47 | 3.33 | 2.36 | 2.92 | 2.28 | 5.99 | 6.77 |
| 10 | 41.87 | 14.69 | 40.86 | 16.24 | 3.27 | 2.32 | 2.86 | 2.23 | 5.98 | 6.77 |
| 11 | 41.69 | 14.72 | 40.71 | 16.29 | 3.25 | 2.28 | 2.86 | 2.18 | 6.04 | 6.83 |
| 12 | 41.98 | 14.63 | 40.95 | 16.24 | 3.24 | 2.38 | 2.87 | 2.29 | 5.95 | 6.74 |
| 13 | 41.68 | 14.64 | 40.73 | 16.16 | 3.29 | 2.28 | 2.90 | 2.20 | 5.99 | 6.75 |
| 14 | 41.92 | 14.77 | 40.75 | 16.36 | 3.25 | 2.30 | 2.86 | 2.21 | 6.03 | 6.85 |
| 15 | 42.06 | 14.59 | 41.19 | 16.12 | 3.24 | 2.34 | 2.85 | 2.26 | 5.96 | 6.72 |
| 16 | 41.74 | 14.56 | 40.83 | 16.14 | 3.22 | 2.33 | 2.87 | 2.23 | 6.01 | 6.77 |
| 17 | 41.83 | 14.71 | 40.76 | 16.37 | 3.29 | 2.27 | 2.92 | 2.19 | 6.01 | 6.81 |
| 18 | 41.78 | 14.75 | 40.60 | 16.31 | 3.23 | 2.35 | 2.86 | 2.24 | 6.02 | 6.83 |
| 19 | 42.03 | 14.60 | 41.15 | 16.12 | 3.24 | 2.31 | 2.85 | 2.21 | 5.95 | 6.72 |
| 20 | 41.85 | 14.71 | 40.79 | 16.24 | 3.34 | 2.26 | 2.95 | 2.15 | 5.98 | 6.77 |
| **Average** | $41.79^{(a)}$ | $14.69^{(b)}$ | $40.78^{(c)}$ | $16.26^{(d)}$ | $3.27^{(a)}$ | $2.31^{(b)}$ | $2.89^{(c)}$ | $2.23^{(d)}$ | $5.99^{(a)}$ | $6.78^{(c)}$ |
| **Relative Performance (%)** | **2.5** | **9.7** | | | **13.3** | **3.9** | | | **11.6** | |

uniform F-18 FDG water phantom injects 3,057.85 Bq/ml and has an acquisition time of 30 min.

The resolution phantom was used to compare the image quality between PDS-OSEM and OP-OSEM. In a human dynamic study, 555 MBq of C-11 Raclopride was injected and several frames were reconstructed with different acquisition times. For real data studies using phantom and human subjects, additional blank scans and transmission scans using the Cs-173 point source were conducted to determine the attenuation correction using the MAP-TR algorithm (Xu et al., 1994, Nuyts et al., 1999). Direct normalization using rotating line Ge-68 source was also applied.

The used reconstructed protocol is based on the OP-OSEM (six iterations, 16 subsets, and matrix of image $256 \times 256$). The OP-OSEM used parameters that are commonly applied to clinical imaging study by HRRT, especially dynamic PET study. In OP-OSEM, the estimated random was obtained by variance reduction on random coincidences (VRR) algorithm, which is designed for HRRT (Byars et al., 2005). VRR is based on the single events based random coincidence estimation (Barker et al., 2004). It estimates the expected random coincidence rate from expected single rates. The expected single rate is obtained by iterative estimation by using the measured delayed coincidences from a delayed coincidence window technique. The scatter sinogram was estimated by the single scatter simulation (SSS) algorithm (Watson, 2000). This algorithm is now one of the most popular methods for scatter correction because of its relatively high level of accuracy. The VRR and SSS implementations used for this study are manufacturer's software provided by Siemens. Hence, both OP-OSEM and PDS-OSEM used the same sinograms to reconstruct PET images. OP-OSEM Eq. (14) reconstructed PET images with random and scatter correction using $n_r^*(d)$ (estimated by VPR) and $n_s^*(d)$ (estimated by SSS) without compensating for $n_p^*(d)$ (prompt sinogram). In contrast, PDS-OSEM Eq. (11) not only iteratively reconstructed PET images using $n_r^*(d)$ and $n_s^*(d)$, but also compensated for $n_p^*(d)$ to perform noise correction Eqs. (12)and (13). The time activity curve (TAC) was used to investigate the fluctuation effects of specified ROIs between PDS-OSEM and OP-OSEM. Both SNR and TAC approaches are used to compare image qualities and performances between PDS-OSEM and OP-OSEM in real dynamic human brain image.

## 3. Results

In the simulation study, we used averaging sum of square error (ASE) to evaluate the difference between estimated ($Est_i$) and true ($Tr_i$) intensity at $i$th pixel, where $i=1, \ldots, B$ (in this case $B$ is the number of pixels in a ROI) as in Eq. (15).

$$ASE = \sum_{i=1}^{B} \frac{[Est_i - Tr_i]^2}{B} \tag{15}$$

Meanwhile, the average (AVG) as in Eq. (16), standard deviation (STD) as in Eq. (17), and signal-to-noise ratio (SNR) of ROI as in Eq. (18) were used to compare the image quality between PDS-OSEM and OP-OSEM.

$$AVG = \sum_{i=1}^{B} Est_i / B \tag{16}$$

$$STD = \sqrt{\frac{1}{B-1} \sum_{i=1}^{B} (Est_i - AVG)^2} \tag{17}$$

$$SNR = \frac{AVG}{STD} \tag{18}$$

Fig. 1 (bottom row) shows the reconstructed images with stopping rules determined by minimum ASE. The smaller ASE means that the reconstructed image resembles the simulated image (Table 1). As shown in Figs. 1–2 and Table 1, it is clear that PDS-OSEM can provide high accuracy, smaller ASE, and higher SNR than OP-OSEM. The averaging relative performances (ARP) indicate that the PDS-OSEM algorithm has a higher accuracy from investigating 20 realizations for the target image. The ARP of SNR and AVG for PDS-OSEM and OP-OSEM in the 1st and 2nd ROIs are (13.3%, 3.9%) and (2.5%, 9.7%), respectively, and the ARP of ASE in both ROIs is 11.6% (Table 1). Especially, PDS-OSEM has a better ARP

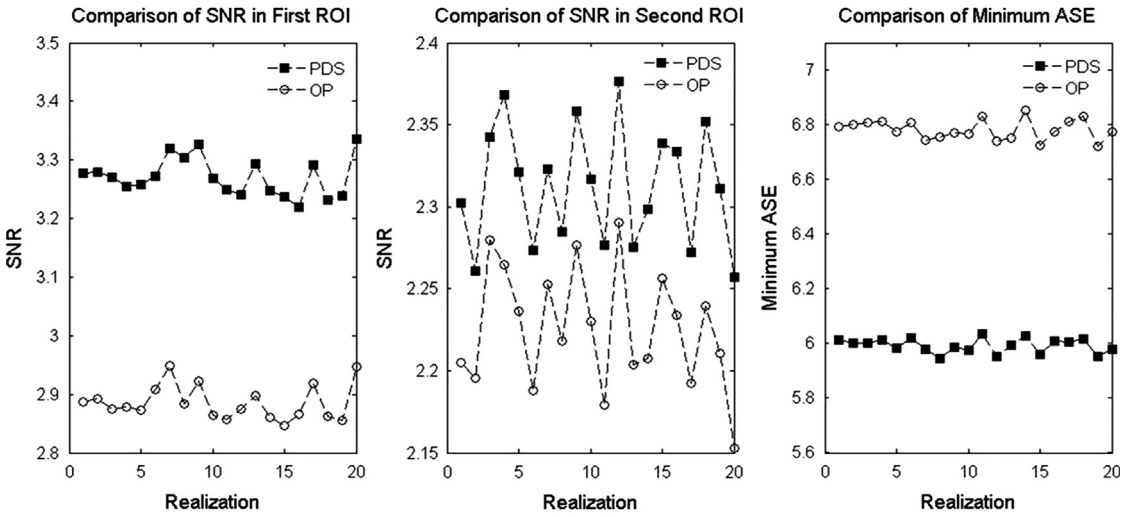


**Fig. 2.** This figure shows SNR and ASE provided by PDS- and OP-OSEM algorithms after 20 realizations.

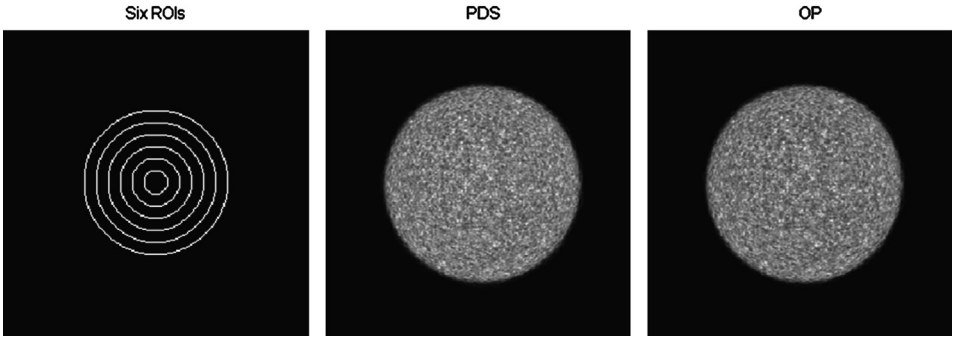


**Fig. 3.** This figure shows the uniform phantom images reconstructed by PDS- and OP-OSEM. The six investigated ROIs were plotted and the radius is 10, 20, 30, 40, 50, and 60 pixels. The SNR of each ROI was used to compare the image quality between PDS- and OP-OSEM from the 43rd to 182nd slices as shown in Fig. 4 and Table 2.

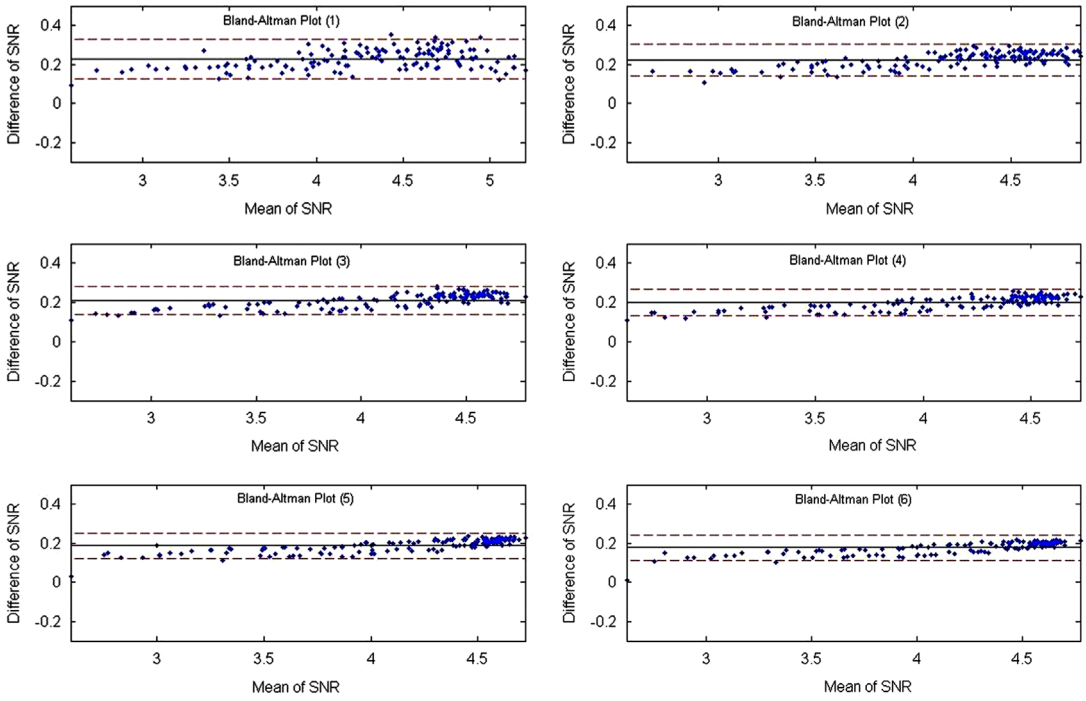


**Fig. 4.** These Bland–Altman plots show comparisons of SNRs between PDS- and OP-OSEM from the 43rd to 182nd slices of uniform phantom images for the six ROIs shown in Fig. 3. The solid lines show the mean $\pm 2 \times$ STD. The *Y*-axis shows the difference of SNRs between PDS- and OP-OSEM. The *X*-axis shows the average SNRs of PDS- and OP-OSEM.

of AVG than that of OP-OSEM in the 2nd ROI, which has lower counts than the 1st ROI.

In the uniform phantom study, the scanning time was 30 min, and 3,057.85 Bq/ml F-18 was injected; 16 subsets and six iterations were used to reconstruct the images. Fig. 3 shows that six SNRs were selected for the SNR comparison between OP- and PDS-OSEM from the 43rd to 182nd slices. The disagreement (Bland–Altman plot (Bland and Altman, 1986)) between PDS- and OP-OSEM indicates that PDS-OSEM has a higher SNR than OP-OSEM (Fig. 4). The mean of the difference between PDS- and OP-OSEM is greater than zero. In Table 2, the *P*-values of the *t*-test display the significantly different mean of SNRs between PDS- and OP-OSEM because all *P*-values are smaller than 0.05. Meanwhile, the SNRs provided by PDS-OSEM are greater than those of OP-OSEM. Hence, the image quality provided by PDS-OSEM is better than that provided by OP-OSEM and contains less noise.

In the resolution phantom, 84,090.91 Bq/ml F-18 was injected, and 16 subsets and six iterations were used to reconstruct images. Fig. 5 shows the resolution phantom images (top-left) reconstructed by OSEM. The central part of the image with 2 mm spacing was used to compare the line profiles between both reconstructed algorithms. The selected locations of vertical line profiles are shown for OP-OSEM at the bottom-left of the image and at the bottom-right for PDS-OSEM. The vertical line profiles (top-right) indicate that PDS-OSEM (green color) has a higher contrast than OP-OSEM (red color) compared with Bland–Altman plots. In a real dynamic human brain study, 555 MBq C-11 Raclopride was injected, and 16 subsets and six iterations were used to reconstruct images. Fig. 6 shows the comparisons of TAC and SNRs between OP-OSEM and PDS-OSEM with the regions of interest (ROI) and the reference (Ref.) in a dynamic human brain study using HRRT. In addition, the increased SNRs of ROI as in Eq. (19) for all the frames are shown.

$$Increased\ SNR = \frac{SNR_{PDS-OSEM} - SNR_{OP-OSEM}}{SNR_{OP-OSEM}} \quad (19)$$

In all frames, SNRs of PDS-OSEM are higher than those of OP-OSEM. The increased SNRs are commonly higher in the early frames, which have shorter scan times (except for the first frame). The higher SNR in the early frames can help obtain more accurate TAC and make it possible to obtain more accurate final parametric imaging. The results of the dynamic study reconstruction show that resultant images produced by PDS-OSEM are more stable and have higher SNRs compared with the OP-OSEM images.

**Table 2**
The *P*-values of *t*-tests are reported for the significant different mean of SNRs from the 43rd to 182nd slices between PDS-OSEM and OP-OSEM, as referred in Fig. 3.

| ROI | PDS-OSEM | | OP-OSEM | | P-value |
|---|---|---|---|---|---|
| | Average | STD | Average | STD | |
| 1 | 4.39 | 0.59 | 4.16 | 0.57 | 1.19E−03 |
| 2 | 4.30 | 0.54 | 4.07 | 0.52 | 4.18E−04 |
| 3 | 4.24 | 0.55 | 4.03 | 0.53 | 9.98E−04 |
| 4 | 4.23 | 0.56 | 4.03 | 0.54 | 2.43E−03 |
| 5 | 4.24 | 0.59 | 4.05 | 0.57 | 6.44E−03 |
| 6 | 4.26 | 0.61 | 4.08 | 0.59 | 1.43E−02 |

## 4. Conclusion

The ASE, SNR, and TAC have been evaluated to compare the accuracy, quality, and feasibility of reconstructing images with the PDS-OSEM and OP-OSEM algorithms via simulated images, empirical phantoms, and real human brain data. The proposed new approach of PDS-OSEM demonstrates less noise, higher

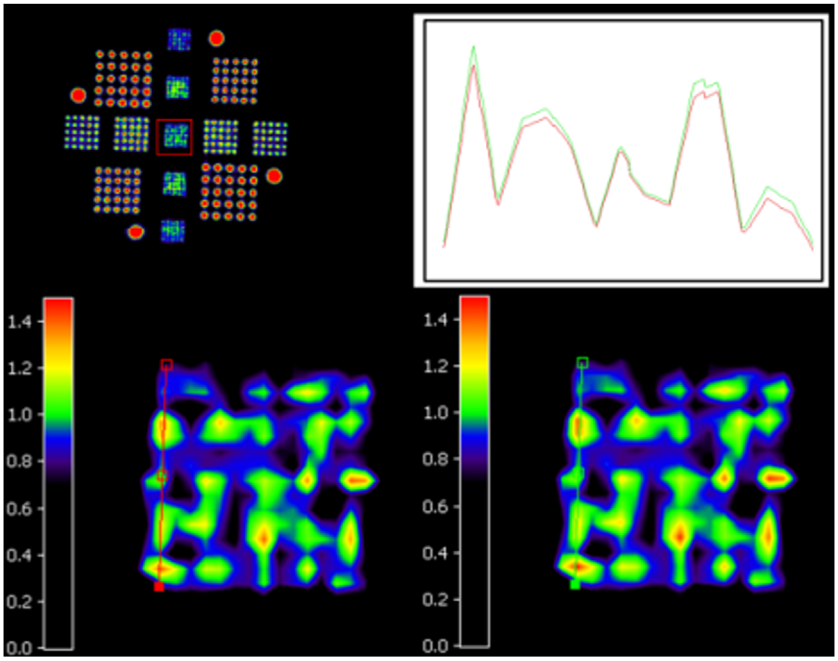


**Fig. 5.** This figure shows resolution phantom images (top-left) reconstructed using the OP-OSEM algorithm. The central part of the reconstructed image was used to compare the image contrast between the two algorithms. The vertical line profile (top-right) was adopted to investigate the image contrast between OP-OSEM (bottom-left and red color) and PDS-OSEM (bottom-right and green color). The vertical line profiles of both algorithms are shown at top-right. They indicate that PDS-OSEM has higher contrast than OP-OSEM. 84,090.91 Bq/ml F-18 was injected; 16 subsets and six iterations were used to reconstruct images.

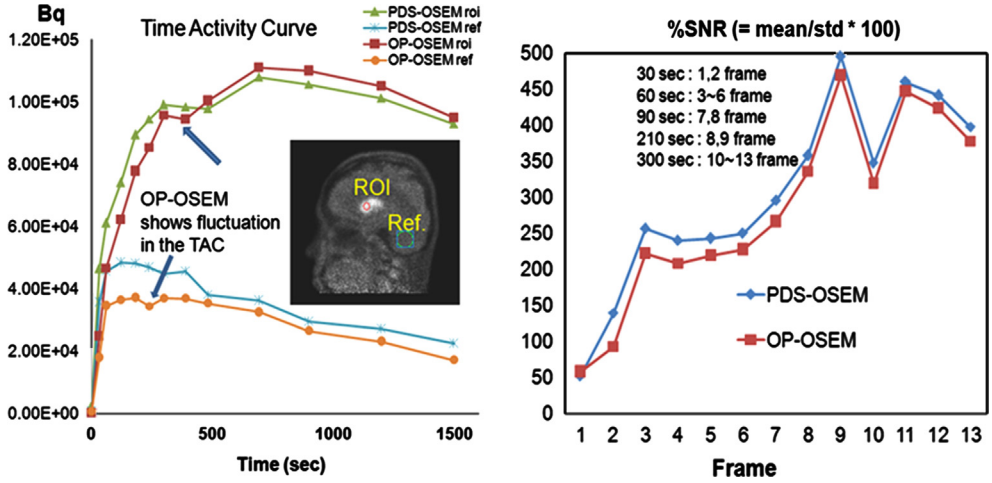


**Fig. 6.** TAC of OP-OSEM and PDS-OSEM with the regions of interest (ROI) and the reference (Ref.) in a dynamic human brain HRRT are shown at top-left. The SNRs of PDS-OSEM are higher than those of OP-OSEM (top-right). The SNRs of ROIs provided by PDS-OSEM and OP-OSEM are increasing in all frames (bottom-right).

accuracy, and higher quality compared with OP-OSEM. The PDS-OSEM algorithm uses the joint Poisson models of prompt, delay, and scatter sinograms based on the MLE-EM algorithm. It has many advantages, such as simplicity in implementation, better maintenance, effectiveness in removing noise, ability to keep positive values, capability of applying to dynamic scanning, and enhancement in image quality without increasing bias and noise. Meanwhile, the PDS-OSEM reconstructs images by iteratively applying random and scatter corrections based on the previously (latest) updated estimates of true events. The proposed method provides a useful approach to estimate true events by the closed form solutions in the derived EM algorithm. The estimate of true events will certainly have less noise. The empirical smoothing techniques cannot distinguish the estimates of random and scatter events. Hence, the presented algorithm provides more accurate information than that of OP-OSEM. Moreover, the proposed method does not need to perform any empirical smoothing step. The presented algorithm can be applied to reconstruct images generated by any PET scanner. However, the PDS-OSEM has increased computational cost. Future work can be conducted to improve PDS-OSEM, including acceleration of the algorithm, combination of attenuation and normalization corrections, selection of initial values for reconstructed algorithm, stopping criterion for iterative scheme, and evaluation of more dynamic studies.

## Acknowledgment

This work was supported by National Science Council (project contract No. NSC 102-2221-E-214-029),, and National Center for Theoretical Sciences, Center of Mathematical Modeling and Scientific Computing at National Chiao Tung University in Taiwan, R. O. C. This research was also supported by the Converging Research Center Program through the Ministry of Science, ICT and Future Planning (2013K000343) and the National Research Foundation (NRF), the Ministry of Education, Science and Technology (2008-2004159), Korea.

## Appendix A

The conditional expectation of the log-likelihood of complete (unobserved) data is derived below. Eqs. (A.1)–(A.5) show the conditional distribution of $n_p(b,d)$, $n_p^r(b,d)$, $n_p^s(b,d)$, $n_r(b,d)$, and $n_s(b,d)$ given as unobserved data followed a binomial distribution where $b=1, \ldots, B$ and $d=1, \ldots, D$.

$$n_p^*(b,d)\Big|n_p^*(d),\lambda_t^k(b),\lambda_r^k(b),\lambda_s^k(b) \sim Bin\left(n_p^*(d),\frac{P(b,d)\lambda_t^k(b)}{\sum_{b'}P(b',d)[\lambda_t^k(b')+\lambda_r^k(b')+\lambda_s^k(b')]}\right), \tag{A.1}$$

$$n_p^r(b,d)|n_p^*(d),\lambda_t^k(b),\lambda_r^k(b),\lambda_s^k(b) \sim Bin\left(n_p^*(d),\frac{P(b,d)\lambda_r^k(b)}{\sum_{b'}P(b',d)[\lambda_t^k(b')+\lambda_r^k(b')+\lambda_s^k(b')]}\right), \tag{A.2}$$

$$n_p^s(b,d)|n_p^*(d),\lambda_t^k(b),\lambda_r^k(b),\lambda_s^k(b) \sim Bin\left(n_p^*(d),\frac{P(b,d)\lambda_s^k(b)}{\sum_{b'}P(b',d)[\lambda_t^k(b')+\lambda_r^k(b')+\lambda_s^k(b')]}\right), \tag{A.3}$$

$$n_r(b,d)|n_r^*(d),\lambda_r^k(b) \sim Bin\left(n_r^*(d),\frac{P(b,d)\lambda_r^k(b)}{\sum_{b'}P(b',d)\lambda_r^k(b')}\right), \tag{A.4}$$

$$n_s(b,d)|n_s^*(d),\lambda_s^k(b) \sim Bin\left(n_s^*(d),\frac{P(b,d)\lambda_s^k(b)}{\sum_{b'}P(b',d)\lambda_s^k(b')}\right). \tag{A.5}$$

Then, Eq. (A.6) shows the conditional expectation of the log-likelihood of complete data (for $\lambda_t^{k+1}(b)$,$\lambda_r^{k+1}(b)$, and $\lambda_s^{k+1}(b)$ at the *next* iteration) given the observed incomplete data and initialized values of parameters ($\lambda_t^k(b)$,$\lambda_r^k(b)$,and $\lambda_s^k(b)$).

$$\begin{aligned}
&Q(\lambda_t(b),\lambda_r(b),\lambda_s(b)|n_p^*,n_r^*,n_s^*,\lambda_t^k(b),\lambda_r^k(b),\lambda_s^k(b))\\
&= E[L(\lambda_t(b),\lambda_r(b),\lambda_s(b))|n_p^*,n_r^*,n_s^*,\lambda_t^k(b),\lambda_r^k(b),\lambda_s^k(b)]\\
&= E\{\sum_d\sum_b\{[n_p^*(b,d)\log(P(b,d)\lambda_t(b))-P(b,d)\lambda_t(b)]\\
&\quad+[n_p^r(b,d)\log(P(b,d)\lambda_r(b))-P(b,d)\lambda_r(b)]\\
&\quad+[n_p^s(b,d)\log(P(b,d)\lambda_s(b))-P(b,d)\lambda_s(b)]\\
&\quad+[n_r(b,d)\log(P(b,d)\lambda_r(b))-P(b,d)\lambda_r(b)]\\
&\quad+[n_s(b,d)\log(P(b,d)\lambda_s(b))-P(b,d)\lambda_s(b)]\}\\
&\quad|n_p^*,n_r^*,n_s^*,\lambda_t^k(b),\lambda_r^k(b),\lambda_s^k(b)\} = \sum_d\sum_b\{\{E[n_p^*(b,d)|n_p^*]\log(P(b,d)\lambda_t(b))\\
&\quad-P(b,d)\lambda_t(b)\}\\
&\quad+\{E[n_p^r(b,d)|n_p^*]\log(P(b,d)\lambda_r(b))-P(b,d)\lambda_r(b)\}\\
&\quad+\{E[n_p^s(b,d)|n_p^*]\log(P(b,d)\lambda_s(b))-P(b,d)\lambda_s(b)\}\\
&\quad+\{E[n_r=(b,d)|n_r^*]\log(P(b,d)\lambda_r(b))-P(b,d)\lambda_r(b)\}\\
&\quad+\{E[n_s(b,d)|n_s^*]\log(P(b,d)\lambda_s(b))-P(b,d)\lambda_s(b)\}\}\\
&= \sum_d\sum_b\{\{A_p(d)\log(P(b,d)\lambda_t(b))-P(b,d)\lambda_t(b)\}
\end{aligned}$$

$$+\{A_r(d)\log(P(b,d)\lambda_r(b))-P(b,d)\lambda_r(b)\}$$
$$+\{A_s(d)\log(P(b,d)\lambda_s(b))-P(b,d)\lambda_r(b)\}$$
$$+\{A_d(d)\log(P(b,d)\lambda_r(b))-P(b,d)\lambda_r(b)\}$$
$$+\{A_c(d)\log(P(b,d)\lambda_s(b))-P(b,d)\lambda_s(b)\}\},\quad (A.6)$$

where

$$A_p(d)=\frac{n_p^*(d)P(b,d)\lambda_t^k(b)}{\sum_{b'}P(b',d)[\lambda_t^k(b')+\lambda_r^k(b')+\lambda_s^k(b')]},\ A_r(d)=\frac{n_p^*(d)P(b,d)\lambda_r^k(b)}{\sum_{b'}P(b',d)[\lambda_t^k(b')+\lambda_r^k(b')+\lambda_s^k(b')]},$$

$$A_s(d)=\frac{n_p^*(d)P(b,d)\lambda_s^k(b)}{\sum_{b'}P(b',d)[\lambda_t^k(b')+\lambda_r^k(b')+\lambda_s^k(b')]},$$

$$A_d(d)=\frac{n_r^*(d)P(b,d)\lambda_r^k(b)}{\sum_{b'}P(b',d)\lambda_r^k(b')},$$

and

$$A_c(d)=\frac{n_s^*(d)P(b,d)\lambda_s^k(b)}{\sum_{b'}P(b',d)\lambda_s^k(b')}.$$

The M-step will determine $\lambda_t^{k+1}(b)$, $\lambda_r^{k+1}(b)$, and $\lambda_s^{k+1}(b)$, the solutions that maximize the function of Eq. (A.6). This can be achieved by taking the first derivatives equal to zero in Eqs. (A.7)–(A.9). The solutions are shown as in Eqs. (A.10)–(A.12).

$$\frac{\partial Q}{\partial\lambda_t(b)}=\sum_d\left\{\frac{A_p(d)}{\lambda_t(b)}-P(b,d)\right\}=0,\Rightarrow\hat{\lambda}_t(b)=\frac{\sum_d A_p(d)}{\sum_d P(b,d)};\quad (A.7)$$

$$\frac{\partial Q}{\partial\lambda_r(b)}=\sum_d\left\{\frac{A_r(d)}{\lambda_r(b)}-P(b,d)+\frac{A_d(d)}{\lambda_r(b)}-P(b,d)\right\}$$
$$=0;\ \Rightarrow\hat{\lambda}_r(b)=\frac{\sum_d[A_r(d)+A_d(d)]}{2\sum_d P(b,d)};\quad (A.8)$$

$$\frac{\partial Q}{\partial\lambda_s(b)}=\sum_d\left\{\frac{A_s(d)}{\lambda_s(b)}-P(b,d)+\frac{A_c(d)}{\lambda_s(b)}-P(b,d)\right\}$$
$$=0;\ \Rightarrow\hat{\lambda}_s(b)=\frac{\sum_d[A_s(d)+A_c(d)]}{2\sum_d P(b,d)}.\quad (A.9)$$

Hence,

$$\lambda_t^{k+1}(b)=\frac{\lambda_t^k(b)}{\sum_{d=1}^D P(b,d)}\sum_{d=1}^D\frac{n_p^*(d)p(b,d)}{\sum_{b'=1}^B p(b',d)[\lambda_t^k(b')+\lambda_r^k(b')+\lambda_s^k(b')]},\quad (A.10)$$

$$\lambda_r^{k+1}(b)=\frac{\lambda_r^k(b)}{2\sum_d P(b,d)}\sum_d\left[\frac{n_p^*(d)P(b,d)}{\sum_{b'=1}^B p(b',d)[\lambda_t^k(b')+\lambda_r^k(b')+\lambda_s^k(b')]}+\frac{n_r^*(d)P(b,d)}{\sum_{b'=1}^B p(b',d)\lambda_r^k(b')}\right],\quad (A.11)$$

$$\lambda_s^{k+1}(b)=\frac{\lambda_s^k(b)}{2\sum_d P(b,d)}\sum_d\left[\frac{n_p^*(d)P(b,d)}{\sum_{b'=1}^B p(b',d)[\lambda_t^k(b')+\lambda_r^k(b')+\lambda_s^k(b')]}+\frac{n_s^*(d)P(b,d)}{\sum_{b'=1}^B p(b',d)\lambda_s^k(b')}\right],\quad (A.12)$$

where $k=1, 2, \ldots, K$, representing the iteration number after the initial number of zero.

The MLE-EM algorithm for the joint model of prompt, delay, and scatter sinograms are described in Eqs. (A.10)–(A12), which is called the *PDS-OSEM* algorithm. This novel approach not only reconstructed HRRT but updated the estimated true intensities with iteratively corrected random and scattering noise.

## References


Astakhov, V., Gumplinger, P., Moisan, C., Ruth, T., Sossi, V., 2003. Effect of depth of interaction decoding on resolution in PET: a simulation study. IEEE Transactions on Nuclear Science 50, 1373–1378.

Byars, L.G., Sibomana, M., Burbar, Z., Jones, J., Panin, V., Barker, W.C., Liow, J.-S., Carson, R.E., Michel, C., 2005. Variance reduction on randoms from delayed coincidence histograms for the HRRT. IEEE NSS 2005 Conference Record, M11–267.

Barker, W.C., Liow, J.-S., Zhao, Y., Thada, S., Iano-Fletcher, A.R., Lenox, M., Michel, C., Johnson, C.A., Carson, R.E., 2004. Randoms estimation for list-mode reconstruction for the ECAT HRRT. IEEE MIC 2004 Conference Record, M9–187.

Barrett, H.H., 1990. Objective assessment of image quality: effects of quantum noise and object variability. Journal of the Optical Society of America A **7**, 1266–1278.

Barrett, H.H., Yao, J., Rolland, J.P., Myers, K.J., 1993. Model observers for assessment of image quality. Proceedings of the National Academy of Sciences, USA 90, 9758–9765.

Barrett, H.H., Denny, J.L., Wagner, R.F., Myers, K.J., 1995. Objective assessment of image quality. II. Fisher information, Fourier crosstalk, and figures of merit for task performance. Journal of the Optical Society of America A 12, 834–852.

Bengel, F.M., Ziegler, S.I., Avril, N., Weber, W., Laubenbacher, C., Schwaiger, M., 1997. Whole-body positron emission tomography in clinical oncology: comparison between attenuation-corrected and uncorrected images. European Journal of Nuclear Medicine 24, 1091–1098.

Bland, J.M., Altman, D.G., 1986. Statistical methods for assessing agreement between two methods of clinical measurement. Lancet 327, 307–310.

Chen, T.-B., Chen, J.-C., Lu, H.H.-S., Liu, R.-S., 2008. MicroPET reconstruction with random coincidence correction via a joint Poisson model. Medical Engineering & Physics 30, 680–686.

Cheng, J.-C.K., Rahmim, A., Blinder, S., Camborde, M.-L., Raywood, K., Sossi, V., 2007. A scatter-corrected list-mode reconstruction and a practical scatter/random approximation technique for dynamic PET imaging. Physics in Medicine & Biology 52, 2089.

Cho, Z.H., Son, Y.D., Kim, H.K., Kim, K.N., Oh, S.H., Han, J.Y., Hong, I.K., Kim, Y.B., 2007. A hybrid PET-MRI: an integrated molecular–genetic imaging system with HRRT-PET and 7.0-T MRI. International Journal of Imaging Systems and Technology 17, 252–265.

Cho, Z.H., Son, Y.D., Kim, H.K., Kim, K.N., Oh, S.H., Han, J.Y., Hong, I.K., Kim, Y.B., 2008. A fusion PET–MRI system with a high-resolution research tomograph-PET and ultra-high field 7.0 T-MRI for the molecular–genetic imaging of the brain. Proteomics 8, 1302–1323.

De Jong, H.W., Van Velden, F.H., Kloet, R.W., Buijs, F.L., Boellaard, R., Lammertsma, A.A., 2007. Performance evaluation of the ECAT HRRT: an LSO–LYSO double layer high resolution, high sensitivity scanner. Physics in Medicine & Biology 52, 1505.

Eriksson, L., Watson, C., Wienhard, K., Eriksson, M., Casey, M., Knoess, C., Lenox, M., Burbar, Z., Conti, M., Bendriem, B., 2005. The ECAT HRRT: an example of NEMA scatter estimation issues for LSO-based PET systems. IEEE Transactions on Nuclear Science 52, 90–94.

Eriksson, L., Wienhard, K., Eriksson, M., Casey, M., Knoess, C., Bruckbauer, T., Hamill, J., Schmand, M., Gremillion, T., Lenox, M., 2002. The ECAT HRRT: NEMA NEC evaluation of the HRRT system, the new high-resolution research tomograph. IEEE Transactions on Nuclear Science, 49; , pp. 2085–2088.

Hong, I., Chung, S., Kim, H., Kim, Y., Son, Y., Cho, Z., 2007. Ultra fast symmetry and SIMD-based projection-backprojection (SSP) algorithm for 3-D PET image reconstruction. IEEE Transactions on Medical Imaging 26, 789–803.

Leroy, C., Comtat, C., Trébossen, R., Syrota, A., Martinot, J.-L., Ribeiro, M.-J., 2007. Assessment of $^{11}$C-PE$_2$I binding to the neuronal dopamine transporter in humans with the high-spatial-resolution PET scanner HRRT. Journal of Nuclear Medicine 48, 538–546.

Nuyts, J., Dupont, P., Stroobants, S., Maes, A., Mortelmans, L., Suetens, P., 1999. Evaluation of maximum-likelihood based attenuation correction in positron emission tomography. IEEE Transactions on Nuclear Science 46, 1136–1141.

Rahmim, A., Cheng, J.-C., Blinder, S., Camborde, M.-L., Sossi, V., 2005. Statistical dynamic image reconstruction in state-of-the-art high-resolution PET. Physics in Medicine & Biology 50, 4887.

Schmand, M., Eriksson, L., Casey, M., Andreaco, M., Melcher, C., Wienhard, K., Flugge, G., Nutt, R., 1998. Performance results of a new DOI detector block for a high resolution PET-LSO research tomograph HRRT. IEEE Transactions on Nuclear Science 45, 3000–3006.

Van Velden, F.H., Kloet, R.W., van Berckel, B.N., Lammertsma, A.A., Boellaard, R., 2009. Accuracy of 3-dimensional reconstruction algorithms for the high-resolution research tomograph. Journal of Nuclear Medicine 50, 72–80.

Van Velden, F.H., Kloet, R.W., van Berckel, B.N., Wolfensberger, S.P., Lammertsma, A.A., Boellaard, R., 2008. Comparison of 3D-OP-OSEM and 3D-FBP reconstruction algorithms for high-resolution research tomograph studies: effects of randoms estimation methods. Physics in Medicine & Biology 53, 3217.

Watson, C.C., 2000. New, faster, image-based scatter correction for 3D PET. IEEE Transactions on Nuclear Science 47, 1587–1594.

Wienhard, K., Schmand, M., Casey, M., Baker, K., Bao, J., Eriksson, L., Jones, W., Knoess, C., Lenox, M., Lercher, M., 2002. The ECAT HRRT: performance and first clinical application of the new high resolution research tomograph. IEEE Transactions on Nuclear Science 49, 104–110.

Xu, M., Luk, W.K., Cutler, P.D., Digby, W.M., 1994. Local threshold for segmented attenuation correction of PET imaging of the thorax. IEEE Transactions on Nuclear Science 41, 1532–1537.